UNIVERSITÀ DI PARMA
ARCHIVIO DELLA RICERCA

University of Parma Research Repository

Extension and application of the Preissmann slot model to 2D transient mixed flows

This is the peer reviewd version of the followng article:

Original
Extension and application of the Preissmann slot model to 2D transient mixed flows / Maranzoni, A., Dazzi, S., Aureli, F., Mignosa, P.. - In: ADVANCES IN WATER RESOURCES. - ISSN 0309-1708. - 82:(2015), pp. 70-82. [doi:10.1016/j.advwatres.2015.04.010]

Availability:
This version is available at: 11381/2797950 since: 2016-08-31T09:39:17Z

Publisher:
Elsevier Ltd

Published
DOI:doi:10.1016/j.advwatres.2015.04.010

Terms of use:

Anyone can freely access the full text of works made available as "Open Access". Works made available

Publisher copyright

note finali coverpage

(Article begins on next page)

12 September 2026

EXTENSION AND APPLICATION OF THE PREISSMANN SLOT MODEL TO 2D TRANSIENT MIXED FLOWS

Andrea Maranzoni[1]; Susanna Dazzi[2]; Francesca Aureli[3]; and Paolo Mignosa[4]

[1] PhD, Researcher, DICATeA, University of Parma, Parco Area delle Scienze 181/A, 43124 Parma, Italy. E-mail: andrea.maranzoni@unipr.it (*Corresponding author*)

[2] PhD Student, DICATeA, University of Parma, Parco Area delle Scienze 181/A, 43124 Parma, Italy. E-mail: susanna.dazzi@studenti.unipr.it

[3] PhD, Researcher, DICATeA, University of Parma, Parco Area delle Scienze 181/A, 43124 Parma, Italy. E-mail: francesca.aureli@unipr.it

[4] PhD, Full Professor, DICATeA, University of Parma, Parco Area delle Scienze 181/A, 43124 Parma, Italy. E-mail: paolo.mignosa@unipr.it

Abstract In this paper, an extension of the Preissmann slot concept is proposed for the modeling of highly transient two-dimensional (2D) mixed flows. The classical conservative formulation of the 2D shallow water equations for free surface flows is adapted assuming that two fictitious vertical slots, aligned along the two Cartesian plane directions and normally intersecting, are added over the ceiling of each integration element. Accordingly, transitions between free surface and pressurized flow can be handled in a natural and straightforward way using the same set of governing equations. The opportunity of coupling free surface and pressurized flows is actually useful not only in one-dimensional (1D) problems concerning sewer systems but also for modeling 2D flooding phenomena in which the pressurization of bridges, culverts, or other crossing hydraulic structures can be expected. Numerical simulations are performed using a shock-capturing, MUSCL-Hancock, finite volume scheme combined with the FORCE (First-Order Centred) solver for the evaluation of the numerical fluxes. The validation of the mathematical model is accomplished on the basis of both exact solutions of 1D discontinuous initial value problems and reference radial solutions of idealized test cases with cylindrical symmetry. Furthermore, the capability of the model to deal with practical field-scale applications is assessed by simulating the transit of a bore under an arch bridge. Numerical results show that the proposed model is suitable for the prediction of highly transient 2D mixed flows.

Keywords: transient mixed flow, numerical modeling, Preissmann slot model, 2D shallow water equations, finite volume method

1. Introduction

Mixed flows are characterized by transitions from free surface to pressurized flow and vice versa, and often occur in the practice in sewers and other closed conduit systems, in which significant variations in flow depth, pressure, and velocity can entail important operational issues and even lead to structural damages (e.g. [17,39]). This is the case of storm water systems, where pressurization may occur when inflow due to intense rainfalls exceeds the pipe capacity. Other notable situations involving mixed flows are pipe filling in water mains, flood propagation in culverted watercourses or under bridges, and transients induced by abrupt operations on hydraulic machineries or gates in pipe networks or in waste and supply pipes of hydroelectric plants.

In the last decades, literature has shown interest towards the analysis of mixed flows, from both experimental and numerical points of view (see, for example, [6,7,25,29,37]), and many efforts have been recently devoted to the development of numerical codes suitable to model this kind of flows (e.g. [3,12,15,33]). Actually, the numerical modeling of transient mixed flows is a very challenging task due to the fact that, in theory, two different sets of governing equations have to be linked at free surface/pressurized flow interfaces. Furthermore, the transition between free surface and pressurized flow can propagate in the form of a hydraulic bore: this requires that numerical schemes are able to accurately resolve discontinuities, avoiding the appearance of spurious post-shock oscillations.

Researchers have mainly focused their attention on the implementation and validation of one-dimensional (1D) numerical models, because the 1D approximation is suitable for most applications (e.g. [8,21,24,30]). However, some practical situations involving mixed flows require a two-dimensional (2D) approximation, at least. This is the case of hydraulic structures, such as bridges and culverts, which may become partially or totally pressurized. In the numerical simulation of flood events in a wide domain, the presence of bridges, culverts, or similar structures is often either neglected (in case these elements do not sensibly affect the flow field) or treated in a simplified way: as an example, Ratia et al. [22] account for the head loss induced by a bridge as an additional source term in a 2D finite volume numerical scheme. For these hydraulic singularities, that are inevitably poorly described in large 2D domains (unless a very high spatial resolution is adopted), 2D/1D dynamically linked modeling has been proposed for an adequate prediction of the near-field effects (e.g. [26]). Anyway, a near-field simulation of the flooding process may require a more accurate description of the flow field around and under bridges or culverts, coupled with a detailed representation of the topography. Moreover, the 1D approximation seems unsuitable for circular or vaulted conduits (such as derivation or by-pass tunnels) in the presence of curves in pipe alignment, when the superelevation in water surface causes a partial wetting of the conduit ceiling. Therefore, it appears that 2D numerical modeling of transient mixed flow deserves attention, but to date, to the best of the author's knowledge, only the study by Van Nam et al. [32] attempted to examine this topic. In that work, original experimental data are provided concerning a steady flow induced in a narrow rectangular culvert placed asymmetrically inside a laboratory flume with rectangular cross-section.

Various approaches have been proposed in literature and are currently available for 1D mixed flow modeling. For an exhaustive critical review, the reader is referred to Bousso et al. [4]. These approaches can be classified into single-equation or two-equation models based on the number of governing equations or, alternatively, into interface tracking models or shock-capturing models based on the methodology of localization of the interface between the two flow regimes. In particular, single-equation models are very simple since they make use of a single set of equations (namely the well-known shallow water equations) for handling both free surface and surcharged flows. The most widely used single-equation model exploits the so-called Preissmann slot concept, originally proposed by Cunge and Wegner [9] according to a Preissmann suggestion. This approach hypothesizes the presence of a fictitious narrow slot over the crown of the conduit. In this way, a surcharged flow is simulated as an open channel flow with the water surface located into the slot and flow pressurization can be modeled on the basis of the open channel flow equations (e.g. [6,10,11,29]). In the case of surcharged flow, the slot induces an additional pressure head and increases the storage capacity of the closed structure, allowing both the compressibility of the flowing liquid and the deformability of the conduit to be taken into account, although in an approximate manner. In practical applications, a very narrow slot is required to simultaneously minimize the volume stored into the slot and to correctly model the pressure wave celerity. However, the slot width is usually set at values in the order of 1-10% of the pipe diameter ([6,10]), since smaller values can lead to numerical instabilities at flow interfaces [36]. In order to overcome this limitation, León et al. [14] suggested to introduce a gradual transition between the pipe and the slot. Moreover, the Preissmann slot approach shows some other important shortcomings. First, it does not allow simulating sub-atmospheric pressurized flows. This problem was addressed by Kerger et al. [11], who proposed to extend the slot below the pipe crown introducing the concept of the "negative" Preissmann slot. Then, the model is not capable to handle air-water interactions and air pocket entrapment, thus it can only be used to perform one-phase simulations and is unsuitable if ventilated conditions are not assured and air pressurization effects cannot be neglected. In these cases, the use of a two-phase model is needed (see, for example, [5,12,30,35]). However, in spite of its limitations, the Preissmann slot model is widely accepted for unsteady mixed flow modeling due to its overall intrinsic simplicity and is often assumed as a reference model to assess the predicting capabilities of new mixed flow solvers (e.g. [34]). Noto and Tucciarelli [20] avoided the Preissmann slot approximation by adopting a special treatment to handle flow regime transitions in a solver based on the decoupling of the 1D unsteady free surface equations into a kinematic and a diffusive component. Similarly, Vasconcelos et al. [33] proposed a single-equation model in which the hydrostatic pressure and the surcharged pressure are decoupled in pressurized flow conditions.

This paper presents a novel 2D single-equation model for simulating transient mixed flows which extends the validity of the 2D shallow water equations to the case of pressurized flows using the Preissmann slot approach. With this aim, each computational cell is expanded over its top by ideally adding two perpendicular narrow slots. The

shallow water equations are solved using the explicit, finite volume, high resolution, Slope Limiter Centred (SLIC) scheme based on the First-Order Centered (FORCE) flux [27]. The model is validated by comparison with exact solutions of 1D discontinuous initial value problems and radial solutions of idealized test cases with cylindrical symmetry. Finally, the suitability of the model to deal with field-scale problems is assessed on the basis of the simulation of the transit of a dam-break bore under an arch bridge.

The paper is organized as follows. In Section 2 the idea underlying the application of the Preissmann slot concept to 2D unsteady mixed flow is presented and the 2D governing equations are derived under the shallow water approximation. Furthermore, the mathematical properties of the equations are discussed. Section 3 is dedicated to the description of the finite volume numerical scheme adopted for solving the modeling equations. In Section 4 a model validation is performed by comparison with theoretical results and a real-scale application is presented. Finally, some concluding remarks are drawn.

2. Mathematical model

The extension of the Preissmann slot concept to 2D modeling is based on the idea of introducing two hypothetical narrow vertical slots on the top of each Cartesian element in which the 2D computational domain is assumed to be discretized. The two slots are aligned along the Cartesian plane directions x and y and extend indefinitely upward (see Fig. 1). In Fig. 1, H denotes the elevation of the ceiling with respect to the bottom; $\Delta x = x_2 - x_1$ and $\Delta y = y_2 - y_1$ indicate the plane dimensions of a generic fixed control element with a rectangular base; T_x and T_y are the widths of the slots along the y- and x-axis directions, respectively. As long as the water surface is below the ceiling, free surface flow occurs and h represents the local water depth; on the contrary, when the water surface reaches the top of the cell, the free surface is inside the slot and the water depth h provides an estimation of the pressure head of an equivalent pressurized flow. Looking again at Fig. 1, A_x and A_y are the flow areas of the x- and y-normal faces respectively, having the shape of rectangular sections with a vertical slot added on the ceiling.

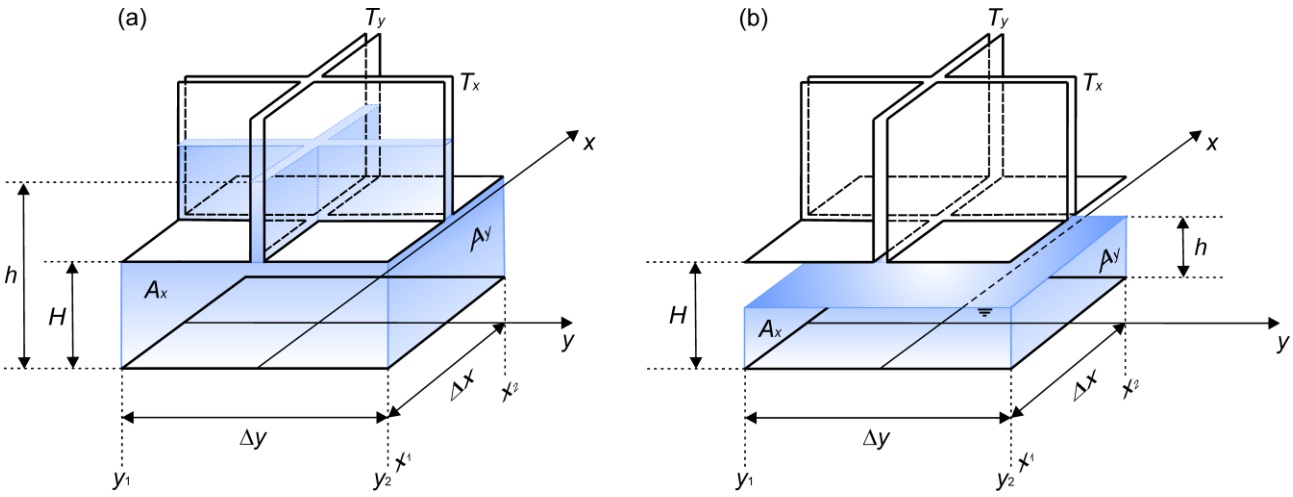

Fig. 1. Definition sketch of the 2D elemental Cartesian control volume with the addition of two narrow vertical slots on the top: flow involving (a) or not involving (b) the slots.

2.1. Governing equations

The conservation mass principle, expressed in the Eulerian form and applied to the case of incompressible flow, states that the rate of change of the total amount of fluid volume V into a control volume equals the net volume rate of flow entering through its boundaries. For the fixed control volume shown in Fig. 1 with planar basis $[x_1, x_2] \times [y_1, y_2]$, this leads to the following basic integral form of the continuity relation:

$$\frac{\partial V}{\partial t} = \left[f(x_1,t) - f(x_2,t)\right] + \left[g(y_1,t) - g(y_2,t)\right], \tag{1}$$

where $f = \int_{A_x} u \, dA_x$ and $g = \int_{A_y} v \, dA_y$ represent the intercell volume fluxes in the x- and y-directions across the lateral faces A_x and A_y respectively, u and v are the x- and y-components of velocity, and t is the time. Introducing the surface-average values $\bar{u}$ and $\bar{v}$ of velocity components over the areas A_x and A_y, the flux functions f and g can be represented as follows:

$$f = \bar{u} A_x, \quad g = \bar{v} A_y. \tag{2}$$

Division of Eq. (1) by the plane area $\Omega = \Delta x \cdot \Delta y$ leads to:

$$\frac{\partial \bar{h}}{\partial t} = \frac{1}{\Delta x}\left[\bar{q}_x(x_1,t) - \bar{q}_x(x_2,t)\right] + \frac{1}{\Delta y}\left[\bar{q}_y(y_1,t) - \bar{q}_y(y_2,t)\right], \tag{3}$$

in which $\bar{h} = \frac{V}{\Omega}$ is the average value of the areal density of water volume over the control element, i.e. a kind of "average water depth" over the planar area Ω, while $\bar{q}_x = \frac{A_x \bar{u}}{\Delta y}$ and $\bar{q}_y = \frac{A_y \bar{v}}{\Delta x}$ are equivalent flow discharges per unit

width along the *x*- and *y*-axis directions, respectively. If the control volume becomes infinitesimal, for smooth solutions Eq. (3) reduces to the differential form:

$$\frac{\partial \bar{h}}{\partial t} + \frac{\partial \bar{q}_x}{\partial x} + \frac{\partial \bar{q}_y}{\partial y} = 0 \,. \tag{4}$$

In addition to mass, momentum is also a "conserved" quantity for the fixed control volume of Fig. 1, and the linear momentum equation can be derived from Newton's second law. In the following, only the *x*-component of the equation will be derived. First, the rate of change of the *x*-momentum within the control volume (CV) can be written as:

$$\frac{\partial}{\partial t}\int_{\mathrm{CV}} \rho u \, dV \approx \frac{\partial}{\partial t}\left(\rho \bar{u} A_x \Delta x\right), \tag{5}$$

assuming that the water mass contained into the slot extending along the *y*-direction does not carry *x*-momentum. In Eq. (5), ρ denotes the water density. Recalling the definition of the equivalent unit discharge $\bar{q}_x$ introduced above, the time derivative in Eq. (5) becomes

$$\frac{\partial}{\partial t}\left(\rho \bar{q}_x \Omega\right). \tag{6}$$

Then, the *x*-component of the convective part of the momentum flux through the faces normal to *x*-axis is:

$$m_c(x_1,t) - m_c(x_2,t)\,, \tag{7}$$

with $m_c = \int_{A_x} \rho u^2 \, dA_x \approx \rho \bar{u}^2 A_x$, while the *x*-momentum carried past the faces normal to *y*-axis becomes:

$$n_c(y_1,t) - n_c(y_2,t)\,, \tag{8}$$

where $n_c = \int_{A_y} \rho u v \, dA_y \approx \rho \bar{u} \bar{v} A_y$. Consequently, the total advective contribution to the momentum flux is:

$$-\rho \Delta y \left(\frac{\bar{q}_x^2}{\bar{h}_x} \right)\Bigg|_{x_1}^{x_2} - \rho \Delta x \left(\frac{\bar{q}_x \bar{q}_y}{\bar{h}_x} \right)\Bigg|_{y_1}^{y_2}, \tag{9}$$

where $\bar{h}_x = \frac{A_x}{\Delta y}$ and $\bar{h}_y = \frac{A_y}{\Delta x}$ represent the surface-average water depths over A_x and A_y, respectively. By assuming a hydrostatic distribution, the pressure term in the *x*-momentum flux reads:

$$m_p(x_1,t) - m_p(x_2,t) = -\left(\rho g \zeta_x A_x\right)\Big|_{x_1}^{x_2}\,, \tag{10}$$

where ζ_x and ζ_y denote the vertical distance of the centroid of the areas A_x and A_y from the water surface, and g the acceleration due to gravity. Finally, the source term includes a component due to gravity:

$$\int_{\mathrm{CV}} \rho g S_{0x} \, dV \approx \left(\rho g A_x S_{0x} \Delta x\right), \tag{11}$$

S_{0x} being the bottom slope in the *x*-axis direction, and a component due to friction:

$$-\rho g A_x S_{fx} \Delta x\,, \tag{12}$$

in which S_{fx} is the friction slope in the *x*-direction. If only bed friction effects are considered, the friction slope can be evaluated by the usual Manning formula:

$$S_{fx} = \frac{n^2 \bar{u}|\bar{u}|}{\bar{h}_x^{4/3}}, \tag{13}$$

where *n* is the Manning roughness coefficient. The mass stored in the *y*-directed slot is assumed not to contribute to the flowing in the *x*-direction, thus is again neglected in the evaluation of contributions (11) and (12). By joining all the previous terms and dividing by ρΩ, the following linear momentum equation can be obtained for the control volume of Fig. 1:

$$\frac{\partial \bar{q}_x}{\partial t} = -\frac{1}{\Delta x}\left(\frac{\bar{q}_x^2}{\bar{h}_x}\right)\Bigg|_{x_1}^{x_2} - \frac{1}{\Delta x}\left(g\zeta_x \bar{h}_x\right)_{x_1}^{x_2} - \frac{1}{\Delta y}\left(\frac{\bar{q}_x \bar{q}_y}{\bar{h}_x}\right)\Bigg|_{y_1}^{y_2} + g\bar{h}_x(S_{0x} - S_{fx}). \tag{14}$$

Ultimately, the application to an infinitesimal control volume gives the *x*-momentum equation written in differential conservation law form:

$$\frac{\partial \bar{q}_x}{\partial t} + \frac{\partial}{\partial x}\left(\frac{\bar{q}_x^2}{\bar{h}_x} + g\zeta_x \bar{h}_x\right) + \frac{\partial}{\partial y}\left(\frac{\bar{q}_x \bar{q}_y}{\bar{h}_x}\right) = g\bar{h}_x(S_{0x} - S_{fx}). \tag{15}$$

Similarly, the *y*-momentum equation can be derived:

$$\frac{\partial \bar{q}_y}{\partial t} + \frac{\partial}{\partial x}\left(\frac{\bar{q}_x \bar{q}_y}{\bar{h}_y}\right) + \frac{\partial}{\partial y}\left(\frac{\bar{q}_y^2}{\bar{h}_y} + g\zeta_y \bar{h}_y\right) = g\bar{h}_y(S_{0y} - S_{fy}). \tag{16}$$

Eqs. (4), (15) and (16) can be combined into a system of equations that can be written using the compact vector notation:

$$\frac{\partial \mathbf{U}}{\partial t} + \frac{\partial \mathbf{F}}{\partial x} + \frac{\partial \mathbf{G}}{\partial y} = \mathbf{S}, \tag{17}$$

in which the vector **U** of the conserved variables, the flux vectors **F** and **G**, and the source term **S** read:

$$\mathbf{U} = \begin{bmatrix} \bar{h} \\ \bar{q}_x \\ \bar{q}_y \end{bmatrix}, \quad \mathbf{F} = \begin{bmatrix} \bar{q}_x \\ \dfrac{\bar{q}_x^2}{\bar{h}_x} + g\zeta_x \bar{h}_x \\ \dfrac{\bar{q}_x \bar{q}_y}{\bar{h}_y} \end{bmatrix}, \quad \mathbf{G} = \begin{bmatrix} \bar{q}_y \\ \dfrac{\bar{q}_x \bar{q}_y}{\bar{h}_x} \\ \dfrac{\bar{q}_y^2}{\bar{h}_y} + g\zeta_y \bar{h}_y \end{bmatrix}, \quad \mathbf{S} = \begin{bmatrix} 0 \\ g\bar{h}_x(S_{0x} - S_{fx}) \\ g\bar{h}_y(S_{0y} - S_{fy}) \end{bmatrix}. \tag{18}$$

Eq. (17), coupled with the previous statements, actually represents a system of modified 2D shallow water equations with a peculiar definition of the set of unknown variables. In particular, the assumption that the water mass flowing in a slot has only a single component of velocity (in the slot direction) ensures that Eq. (17) shows the classical structure of the 2D shallow water equations with the first terms of the **F** and **G** flux vectors coinciding respectively with the second and third component of the vector **U** of the conserved variables. If $h < H$, then the water surface is below the ceiling, $\bar{h}$

reduces to h (the same holds for $\bar{h}_x$ and $\bar{h}_y$), and Eq. (17) returns to the usual system of the 2D shallow water equations (e.g., [28]). The geometrical properties of the control volume can be easily extended for $h \geq H$ considering the addition of two crossing vertical slots on the top with dimensionless width $k_x = T_x/\Delta x$ and $k_y = T_y/\Delta y$, respectively:

$$V = \begin{cases} \Omega h & \text{for } 0 \leq h < H \\ \Omega H \left[1 + (k_x + k_y - k_x k_y) \left(\frac{h}{H} - 1 \right) \right] & \text{for } h \geq H \end{cases}, \quad \bar{h} = \begin{cases} h & \text{for } 0 \leq h < H \\ H \left[1 + (k_x + k_y - k_x k_y) \left(\frac{h}{H} - 1 \right) \right] & \text{for } h \geq H \end{cases}, \tag{19}$$

$$A_x = \begin{cases} \Delta y\, h & \text{for } 0 \leq h < H \\ \Delta y\, H \left[1 + k_y \left(\frac{h}{H} - 1 \right) \right] & \text{for } h \geq H \end{cases}, \quad \bar{h}_x = \begin{cases} h & \text{for } 0 \leq h < H \\ H \left[1 + k_y \left(\frac{h}{H} - 1 \right) \right] & \text{for } h \geq H \end{cases}, \tag{20}$$

$$\zeta_x \bar{h}_x = \begin{cases} \frac{h^2}{2} & \text{for } 0 \leq h < H \\ H \left(h - \frac{H}{2} \right) + \frac{(h-H)^2}{2} k_y & \text{for } h \geq H \end{cases}. \tag{21}$$

Similar expressions can be derived for A_y, $\bar{h}_y$, and $\zeta_y \bar{h}_y$. It can be noticed that these geometrical quantities are continuous functions of h, with a discontinuity in the derivative at $h = H$. This sudden change in the gradient is more severe for narrower slots.

Therefore, by the simple generalization of the classic Preissmann slot model above described, a 2D mixed flow can be easily modeled as an equivalent 2D free surface flow occurring in a fixed integration element with peculiar composite shape, without the need of special treatments for handling transitions between free surface and pressurized conditions. In this way, it is possible to extend to the 2D modeling the capability of dealing with the surcharging of the system, without modifying the governing equations. The high celerity values typical of the pressure waves can be reproduced through a suitable setting of the slot widths. Finally, Eq. (17) easily reduces to the x- (or y-) split 2D shallow water equations when the velocity component in the y- (or x-) direction vanishes; in this case, the classical 1D geometrical schematization of the Preissmann slot model can be obtained if the width of the transverse slot is set to zero.

2.2 Properties of the equations

In this subsection, the eigenstructure of the governing equations is analyzed with respect to the conserved variables [28]. For $h \geq H$, the Jacobian matrix $\mathbf{J_F}$ corresponding to the flux vector $\mathbf{F}$ defined in Eq. (18) is given by:

$$\mathbf{J_F} = \begin{bmatrix} 0 & 1 & 0 \\ \left\{-\left(\frac{\bar{q}_x}{\bar{h}_x}\right)^2 + gH\left[\frac{1}{k_y} + \left(\frac{h}{H} - 1\right)\right]\right\} \frac{k_y}{k_x + k_y - k_x k_y} & 2\frac{\bar{q}_x}{\bar{h}_x} & 0 \\ -\frac{\bar{q}_x \bar{q}_y}{\bar{h}_y^2} \frac{k_x}{k_x + k_y - k_x k_y} & \frac{\bar{q}_y}{\bar{h}_y} & \frac{\bar{q}_x}{\bar{h}_y} \end{bmatrix}, \tag{22}$$

while, for $h < H$, it reduces to the familiar form typical of the 2D shallow water equations:

$$\mathbf{J_F} = \begin{bmatrix} 0 & 1 & 0 \\ -\bar{u}^2 + gh & 2\bar{u} & 0 \\ -\bar{u}\bar{v} & \bar{v} & \bar{u} \end{bmatrix}. \tag{23}$$

The eigenvalues of $\mathbf{J_F}$ (Eq. 22) can be obtained after some algebra:

$$\lambda_1 = \bar{u} - c_x, \quad \lambda_2 = \frac{\bar{q}_x}{\bar{h}_y}, \quad \lambda_3 = \bar{u} + c_x, \tag{24}$$

where the celerity c_x is a function of both h and $\bar{u}$ (for $h \geq H$):

$$c_x = \sqrt{\bar{u}^2 - \left\{\bar{u}^2 - gH\left[\frac{1}{k_y} + \left(\frac{h}{H} - 1\right)\right]\right\} \frac{k_y}{k_x + k_y - k_x k_y}}. \tag{25}$$

For the special case of $k_x = k_y = k$, the celerity is

$$c_x = \sqrt{\bar{u}^2 \frac{1-k}{2-k} + gH \frac{1}{2-k}\left[\frac{1}{k} + \left(\frac{h}{H} - 1\right)\right]}, \tag{26}$$

k and H acting as geometric parameters. Moreover, in the particular case of a 1D flow along the x-direction, assuming k_x equal to zero in Eq. (25), c_x becomes a function of h only:

$$c_x = \sqrt{gH\left[\frac{1}{k_y} + \left(\frac{h}{H} - 1\right)\right]}. \tag{27}$$

It can be easily verified that expression (27) is equivalent to the usual celerity formula $c = \sqrt{gA/b}$ (where A is the flow area and b the free surface width) applied to a composite rectangular section with the addition of a vertical slot over the crown. For $h = H$, Eq. (27) shows a discontinuity in the celerity value that can be very strong for low values of k. As highlighted in various studies of literature, this is the main cause of the significant spurious oscillations that usually affect numerical results at strong transitions between free surface and pressurized flow (e.g. [36]).

Similar analysis can be performed for the Jacobian matrix $\mathbf{J_G}$ corresponding to the flux $\mathbf{G}$.

It is well known that the classic 2D shallow water equations are strictly hyperbolic for a wet bed. The strict hyperbolicity of Eq. (17) is confirmed even for $h \geq H$, since the Jacobian matrices $\mathbf{J_F}$ and $\mathbf{J_G}$ admit three real eigenvalues which, in addition, are all distinct.

3. Numerical scheme

The time-dependent 2D system of equations (17) can be efficiently solved by adopting finite volume schemes (e.g. [16,27]). Among these, high resolution schemes are widely used in literature, both in unsteady open channel (e.g. [28]) and in water hammer problems (e.g. [23,38]), due to their shock-capturing property. The application of Godunov-type numerical methods is usual also for the simulation of 1D transient mixed flows in storm sewers (e.g. [4,11,13,14,24,33]).

In this paper, Eq. (17) is discretized over a uniform Cartesian grid with dimensions $\Delta x \times \Delta y$ using the following explicit finite volume scheme, based on the Strang splitting of the source term [27]:

$$\begin{aligned}
\mathbf{U}_{i,j}^{*} &= \mathbf{U}_{i,j}^{n} + \frac{\Delta t}{2}\mathbf{S}_{i,j}^{n} \\
\mathbf{U}_{i,j}^{**} &= \mathbf{U}_{i,j}^{*} - \frac{\Delta t}{\Delta x}\left[\mathbf{F}_{i+1/2,j} - \mathbf{F}_{i-1/2,j}\right] - \frac{\Delta t}{\Delta y}\left[\mathbf{G}_{i,j+1/2} - \mathbf{G}_{i,j-1/2}\right] \\
\mathbf{U}_{i,j}^{n+1} &= \mathbf{U}_{i,j}^{**} + \frac{\Delta t}{2}\mathbf{S}_{i,j}^{**}.
\end{aligned} \tag{28}$$

According to this succession of updates, the cell-average $\mathbf{U}_{i,j}$ in the i,j-cell evolves from the time level n to the time level n+1 (being $\Delta t = t^{n+1} - t^{n}$ the computational time interval). In a single step, both x and y fluxes are taken into account through the intercell numerical fluxes $\mathbf{F}_{i\pm1/2,j}$ and $\mathbf{G}_{i,j\pm1/2}$ (in the x and y directions, respectively) calculated at the intermediate state $\mathbf{U}^{*}$. Forcing effects are involved by the cell-averaged source term vector $\mathbf{S}_{i,j}$ that in Eq. (28) is evaluated at the states $\mathbf{U}^{n}$ and $\mathbf{U}^{**}$.

The Slope Limiter Centred (SLIC) scheme proposed by Toro [27] is here adopted, coupled with the classic slope limiter function of Van Leer [31]. In the framework of this method, the numerical fluxes are evaluated by the First-Order Centred (FORCE) flux [27]. The intercell boundary values of the variables A_x, $\bar{h}_x$, and $\zeta_x \bar{h}_x$ (similarly for A_y, $\bar{h}_y$, and $\zeta_y \bar{h}_y$) are reconstructed on the basis of the geometrical relations (20)-(21).

This numerical procedure for solving the homogeneous problem is theoretically second-order accurate in space and time. With regard to stability, the explicit, unsplit MUSCL-Hancock scheme applied to the 2D linear advection equations with constant velocity components $a_x > 0$ and $a_y > 0$ (in the x and y directions, respectively) has the stability range [27]:

$$a_x \frac{\Delta t}{\Delta x} + a_y \frac{\Delta t}{\Delta y} \le 1. \tag{29}$$

The extension of this condition to the non-linear problem (17)-(18) leads to the stability restriction:

$$\max_{i,j}\left[\left(\left|\frac{\bar{q}_x}{\bar{h}_x}\right| + c_x\right)\frac{\Delta t}{\Delta x} + \left(\left|\frac{\bar{q}_y}{\bar{h}_y}\right| + c_y\right)\frac{\Delta t}{\Delta y}\right] \le 1, \tag{30}$$

involving the wave speeds c_x and c_y of the hyperbolic system. The condition expressed by Eq. (30) is certainly satisfied if the computational time step Δt is calculated as follows:

$$\Delta t = \frac{1}{2} Cr \min_{i,j} \left(\frac{\Delta x}{\left| \frac{\overline{q}_x}{\overline{h}_x} \right| + c_x} , \frac{\Delta y}{\left| \frac{\overline{q}_y}{\overline{h}_y} \right| + c_y} \right), \tag{31}$$

where Cr denotes the Courant number (≤ 1).

The effectiveness and robustness of this numerical method for solving 2D shallow water equations in dam-break modeling have been extensively tested by the authors on the basis of both analytical and real field test cases (see, for example, [2]).

4. Numerical tests

In this section the model previously described is validated by comparing numerical results with both exact solutions of 1D discontinuous initial value problems and reference radial solutions of idealized test cases with cylindrical symmetry. All validation tests concern frictionless problems with horizontal bathymetry. Finally, an application to a field-scale dam-break case is presented.

4.1. 1D test cases with exact solution

The capability of the numerical model to simulate highly transient mixed flows is first assessed on the basis of some 1D test problems with exact solution. Valuable solutions in the framework of unsteady mixed flow modeling can be obtained by exploiting the exact Riemann solver proposed by Kerger et al. [11] for the homogeneous de Saint-Venant equations, in analogy with the general solution strategy of the Riemann problem for the x-split 2D shallow water equations [28]. This exact solver was there employed to evaluate intercell fluxes in a Godunov-type scheme for the simulation of transient mixed flows in circular and rectangular pipes with the addition of a Preissmann slot on the top. The same solver is here used to calculate reference exact solutions for 1D initial value problems with piecewise constant initial states $\mathbf{U}_\mathrm{L}$ (on the left side) and $\mathbf{U}_\mathrm{R}$ (on the right side).

All tests consider a 20 m-long frictionless and horizontal duct characterized by a rectangular cross-section with height H and width B both equal to 1 m. The computational domain $[-10, 10]$ m $\times$ $[0, 1]$ m is discretized by means of $n_x = 2000 \times n_y = 10$ rectangular cells with size $\Delta x = 0.01$ m $\times$ $\Delta y = 0.1$ m. Since each computational cell is provided with two fictitious vertical slots aligned along the two plane directions x and y, the closed conduit presents n_y longitudinal slots in place of the classic single slot that is ideally introduced on the pipe crown when the slot concept is applied to the 1D equations. The width T_y of the slots in the longitudinal direction is assumed to be equal to a suitable

fraction of the cross-sectional grid size Δy ($k_y = T_y/\Delta y$). Therefore, an array of longitudinal slots with fixed dimensionless width k_y conceptually replaces a single slot with the same value of the ratio of slot width to conduit width. Moreover, in the simulation of 1D problems, the dimensionless width of the transverse slots ($k_x = T_x/\Delta x$) should be assumed sufficiently small in order to limit the artificial increase in the pipe volume. Table 1 summarizes the test conditions and gives the initial left and right values for the three test cases considered (in the following, the overbar above the velocity components is omitted for simplicity). The discontinuity in the initial states is located at the origin of the x-axis. In all the simulations, the stability condition stated by Eq. (31) is adopted with the Courant number Cr equal to 0.9.

Table 1 Test conditions for three 1D discontinuous initial-value problems with exact solution (computational domain defined by [−10, 10] m × [0, 1] m and initial discontinuity located at x = 0 m).

Test	h_L (m)	u_L (m/s)	h_R (m)	u_R (m/s)	H (m)	Description
1a	0.8	2.0	0.8	−2.0	1.0	Two transition shocks
1b	3.0	0.0	0.5	0.0	1.0	Left transition rarefaction and right shock
1c	1.5	1.0	1.5	−1.0	1.0	Two water hammer waves

Test 1a is characterized by an initial condition representing two colliding uniform free-surface flows with the same water depth but opposite velocities. The impingement of the two incoming flows produces a pressurized intermediate state which expands thanks to two transition shock waves travelling in opposite directions. If only one half of the domain is considered, this situation is equivalent to the propagation of a pipe-filling surge originated by the sudden closure of the downstream end of a conduit. The two states across the travelling discontinuity are connected by the Rankine-Hugoniot jump conditions (e.g. [16]). In Fig. 2, two analytical profiles (at t = 0.5 s and t = 1.0 s) of both pressure head and velocity, obtained using the Rankine-Hugoniot relations ($T_y = 0$), are compared with the corresponding profiles predicted by the exact Riemann solver of Kerger et al. [11] for different values of the slot width. In particular, Table 2 shows the influence of the Preissmann slot width on the accuracy of the exact solver in predicting the pressure head h^* and velocity u^* in the intermediate (star) region, as well as the shock wave speed s_x. Moreover, for the two times considered, Table 2 reports information about the volume fraction stored within the slot compared to the overall, instantaneous water volume contained in the duct. The introduction of the Preissmann slot, due to the additional volume made available, noticeably affects both the propagation speed and the strength of the reflected surge: in fact, wave celerity and jump height decrease with the increasing of the slot width. The Preissmann slot model seems capable to accurately describe the propagation of the transition wave as long as the slot is narrow enough to guarantee that the water volume contained within the slot is negligible with respect to the overall water volume. However, a conveniently

wide slot is typically adopted in urban drainage modeling (often around 1-10% of the conduit width) in order to enforce non-oscillating results. In this work, a dimensionless slot width k_y of 0.01 is preferably assumed, as a reasonable compromise between accuracy and computational stability. For Test 1a, a computational time step in the order of 10^{-4} s derives from this choice. Fig. 3 compares the numerical results of two simulations carried out by setting k_y to 0.01 and 0.1 (k_x = 0.001 for both simulations) with the corresponding 1D solutions obtained from the exact Riemann solver by considering a longitudinal slot with the same dimensionless width. The numerical model seems to correctly resolve the abrupt transition between free surface and surcharged regimes. However, spurious oscillations appear behind the shock wave. Literature review confirms that these numerical instabilities systematically arise near sharp pipe filling bores, even if high resolution schemes are adopted, due to the strong increase of the wave celerity when the flow involves the slot (e.g. [36]). Fig. 3 shows that the strength of the numerical oscillations at flow transitions slightly depends on the slot width.

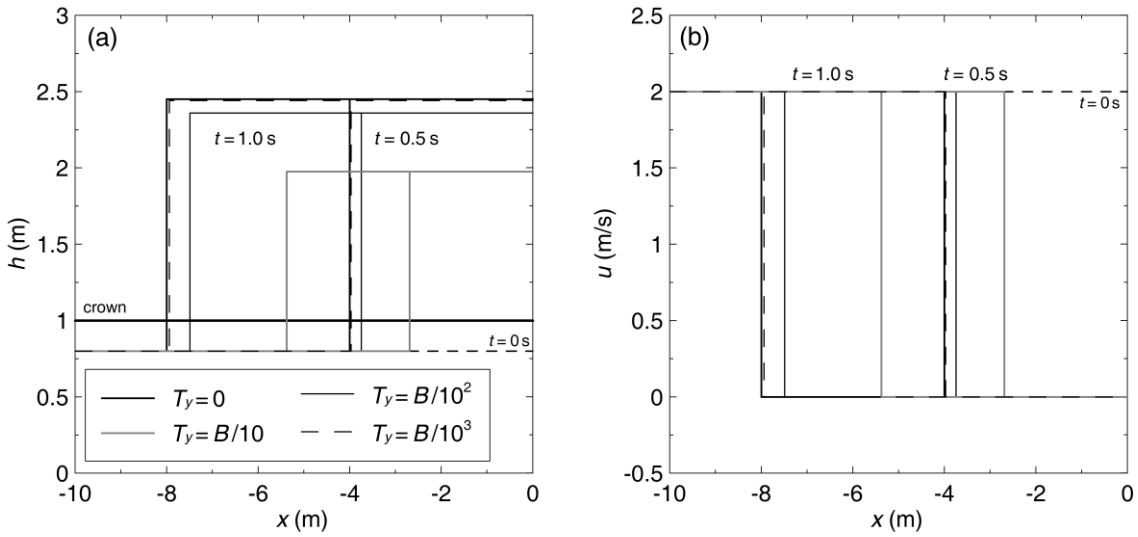

Fig. 2. Test 1a: exact solutions at t = 0.5 s and t = 1.0 s calculated with different values of the slot width (channel width B = 1 m); (a) pressure head, (b) velocity. T_y = 0 refers to the solution obtained by applying the Rankine-Hugoniot relations. The other theoretical profiles are computed using an exact Riemann solver. Only the sub-domain [–10, 0] m is represented for clarity.

Table 2 Test 1a: sensitivity of the solution provided by the exact Riemann solver by Kerger et al. [11] to the width of the Preissmann slot. Relative percent deviations are referred to the analytical solution derived from the application of the Rankine-Hugoniot conditions. The volume fraction contained within the slot with respect to the overall water volume in the duct is reported for t = 0.5 s and t = 1.0 s.

T_y / B (-)	Δh^* (%)	Δu^* (%)	Δs_x (%)	$V_{\text{slot}\ (t = 0.5\ \text{s})}$ (%)	$V_{\text{slot}\ (t = 1.0\ \text{s})}$ (%)
10^{-3}	–0.43	0.0	–0.71	0.07	0.12
10^{-2}	–3.76	0.0	–6.36	0.58	1.06

10^{-1}	−19.40	0.0	−32.80	2.98	5.47

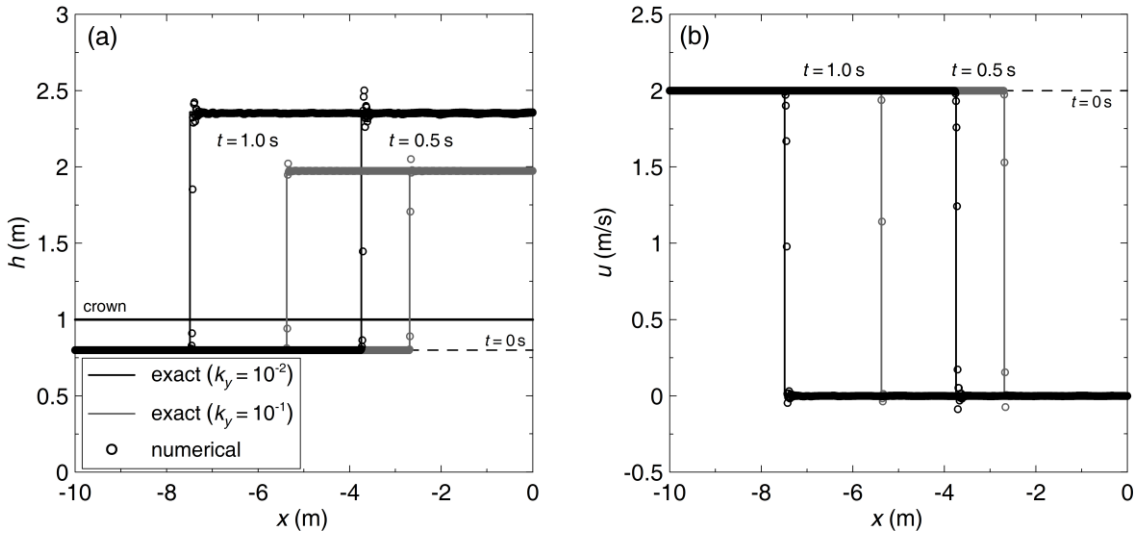

Fig. 3. Test 1a: comparison between theoretical solution provided by the exact Riemann solver and numerical results at t = 0.5 s and t = 1 s; (a) pressure head, (b) velocity. Two data series are reported, corresponding to k_y = 0.01 and k_y = 0.1 respectively (settings of the model parameters: Δx = 0.01 m, k_x = 0.001, Δy = 0.10 m, Cr = 0.9). Only the sub-domain [−10, 0] m is represented for clarity.

On the basis of the same test conditions (Test 1a), a sensitivity analysis is carried out in order to highlight the effect of the longitudinal mesh size Δx on the numerical results. Fig. 4 compares pressure head and velocity profiles at t = 0.5 s extracted from three different simulations performed with Δx = 0.01, 0.05, and 0.1 m. All the other model parameters are unchanged. The numerical model shows a slight shift in the location of the discontinuity. Furthermore, it spreads the discontinuity over a small number of grid cells, which seems not to be influenced by Δx. For this reason, the numerical profiles appear the more diffusive the coarser is the mesh. Analogously, the finer is the mesh, the shorter is the space interval along which spurious oscillations at the transition front vanish. Moreover, oscillation amplitude seems insensitive to grid size. The deviation of the numerical pressure head and velocity profiles from the reference solution provided by the exact Riemann solver can be quantified by the L_1-error, commonly used for conservation laws [16]:

$$E_{L_1}(h) = \Delta x \sum_i \left| h_{num} - h_{exact} \right|, \quad E_{L_1}(u) = \Delta x \sum_i \left| u_{num} - u_{exact} \right|. \tag{32}$$

Table 3 reports the results obtained for t = 0.5 s considering the half computational domain [−10, 0] m. It can be noticed that grid refinement induces a reduction of the pressure head error. On the contrary, the overall error in the velocity profile is slightly affected by the grid spacing in the Δx-range considered. Anyway, these errors are mainly attributable to the numerical approximation in the reconstruction of the transition bore.

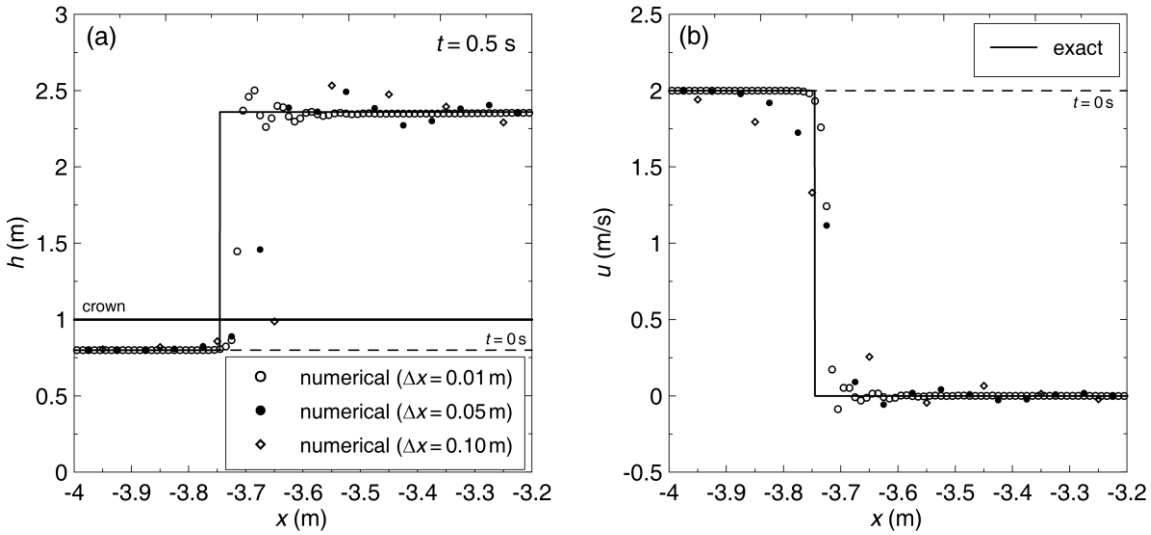

Fig. 4. Test 1a: convergence analysis based on three different longitudinal grid sizes (Δx = 0.01, 0.05, and 0.10 m). Pressure head (a) and velocity (b) profiles at t = 0.5 s are shown (k_x = 0.001, Δy = 0.10 m, k_y = 0.01, Cr = 0.9). The x-axis is limited to the interval [−4, −3.2] for clarity.

Table 3 Test 1a: sensitivity analysis on longitudinal grid size based on the pressure head and velocity profiles at t = 0.5 s. The L_1-norms are calculated with respect to the exact solution over the half computational domain [−10, 0] m.

Δx (m)	$E_{L_1}(h)$ (m^2)	$E_{L_1}(u)$ (m^2/s)
0.01	0.8407	0.5567
0.05	0.9030	0.5591
0.10	0.9803	0.5589

The sensitivity of the numerical results to the width of the transverse slot can be assessed looking at Fig. 5, in which three pressure head and velocity profiles at t = 0.5 s, computed using three different values of the dimensionless slot width k_x (10^{-2}, 10^{-3} and 10^{-4}), are compared with the exact solution (k_y = 0.01). Since the reference 1D solution does not take into account the fictitious increment of the conduit volume induced by the system of transverse slots, it can be expected that the agreement between reference and numerical solutions improves with decreasing k_x. This trend is evident in Table 4 which shows the deviation between predicted and reference pressure head and velocity profiles at t = 0.5 s, estimated through the L_1-norm defined in Eq. (32) for the half domain [−10, 0] m. Actually, the pipe filling bore is well reproduced provided that k_x is set at least one/two orders of magnitude less than k_y. If the width of the transverse slot is assumed of the same order of magnitude as the longitudinal one, the celerity of the sharp transition wave is underestimated, as well as the height of the jump in pressure head caused by the wave transit.

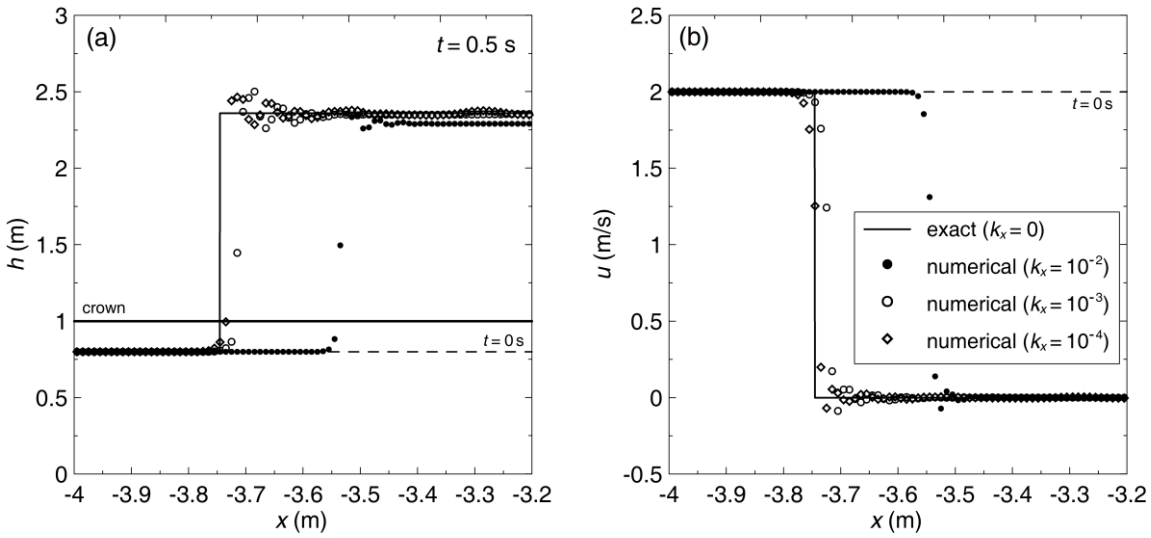

Fig. 5. Test 1a: sensitivity analysis with respect to the width of the transverse slot ($k_x = 10^{-2}$, 10^{-3}, and 10^{-4}). Pressure head (a) and velocity (b) profiles at $t = 0.5$ s are shown ($\Delta x = 0.01$ m, $\Delta y = 0.10$ m, $k_y = 0.01$, $Cr = 0.9$). The x-axis is limited to the interval [−4, −3.2] for clarity.

Table 4 Test 1a: sensitivity analysis on the parameter k_x based on the pressure head and velocity profiles at $t = 0.5$ s ($k_y = 0.01$). The L_1-norms are calculated with respect to the exact solution over the half computational domain [−10, 0] m.

k_x (m)	$E_{L_1}(h)$ (m^2)	$E_{L_1}(u)$ (m^2/s)
10^{-4}	0.7880	0.5184
10^{-3}	0.8407	0.5567
10^{-2}	1.3235	0.9158

Test 1b represents a sort of "dam-break" problem in which a wall (located at $x = 0$ m) initially separates a pressurized left state from a free surface right state (see Table 1). The solution consists of a free surface shock wave propagating downstream and a left rarefaction wave along which a smooth transition between free surface and pressurized flow occurs (Fig. 6). This transition rarefaction wave appears very steep in the pressurized portion and shows a considerable spread in correspondence to the flow transition. This behaviour is due to the fact that the left eigenvalue is practically constant where the flow is pressurized and strongly changes across the crown of the closed conduit. Fig. 6 shows pressure head and velocity profiles at $t = 0.3$ s computed on the basis of two different values of the model parameter k_x ($k_x = 10^{-3}$ and 10^{-4}). The numerical profiles (especially in the portion corresponding to the rarefaction wave) are rather sensitive to the dimensionless slot width k_x, and a good agreement with the solution of the exact Riemann solver is achieved with $k_x = 10^{-4}$. The free surface intermediate state located between the two waves (star region) is well

reproduced by the numerical model. With reference to these simulations not involving inflow or outflow contributions, at $t = 0.3$ s, after approximately two thousands computational time steps, the relative volume conservation error (with respect to the initial water volume) is in the order of 10^{-13}, independently from the value of k_x. Table 4 provides quantitative information on the overall accuracy of the numerical reconstruction of pressure head and velocity profiles at $t = 0.3$ s for different longitudinal grid sizes. The L_1-error norms, calculated by applying Eq. (32) over the total domain [−10, 10] m, show a trend towards pointwise convergence of the numerical profiles to the reference solution as the grid is refined. In particular, if too coarse a mesh is adopted, an excessive numerical spreading of the rarefaction and shock waves occurs, with strong inaccuracy in the prediction of the intermediate state in the star region.

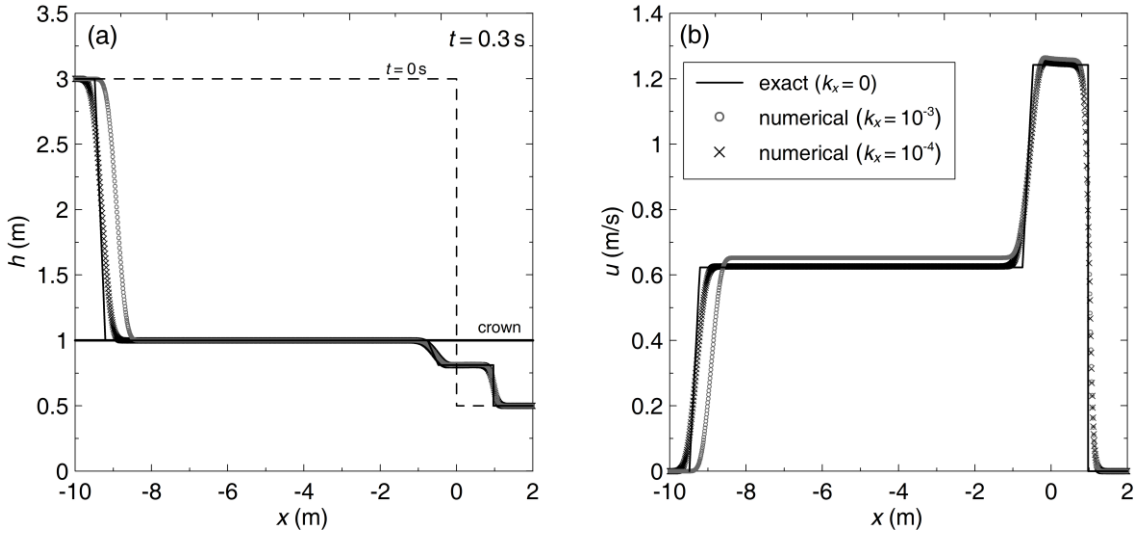

Fig. 6. Test 1b: comparison between exact solution and numerical results at $t = 0.3$ s ($\Delta x = 0.01$ m, $\Delta y = 0.10$ m, $k_y = 0.01$, $Cr = 0.9$); (a) pressure head, (b) velocity. Profiles obtained by setting two different widths for the transverse slot ($k_x = 10^{-3}$ and 10^{-4}) are shown. Only the sub-domain [−10, 2] m is represented for clarity.

Table 5 Test 1b: sensitivity analysis on longitudinal grid size based on the pressure head and velocity profiles at $t = 0.3$ s ($k_y = 10^{-2}$, $k_x = 10^{-4}$). The L_1-norms are calculated with respect to the exact solution over the total computational domain [−10, 10] m.

Δx (m)	$E_{L_1}(h)$ (m^2)	$E_{L_1}(u)$ (m^2/s)
0.01	0.2234	0.2319
0.05	0.5511	0.6015
0.10	0.8069	0.8454

Finally, Test 1c involves a fully pressurized flow and aims at assessing the capability of the model to simulate water hammer transients. Initial data refer to two colliding pressurized flows moving with opposite velocities in a rectangular

duct. The same test can simulate the stopping of a pressurized uniform flow caused by the instantaneous closure of a downstream valve. A Preissmann slot with a size of 0.001% of the conduit width is adopted, thus the propagating pressure wave is modelled by means of a gravity wave travelling with a celerity of approximately 990 m/s. This value is realistic in water hammer phenomena. Fig. 7 shows numerical pressure head and velocity profiles at $t = 0.003$ s and $t = 0.008$ s, and the reference solution derived from the exact Riemann solver. The reference solution is accurately reproduced by the numerical model and, in particular, the water hammer wave is well resolved without the appearance of spurious oscillations.

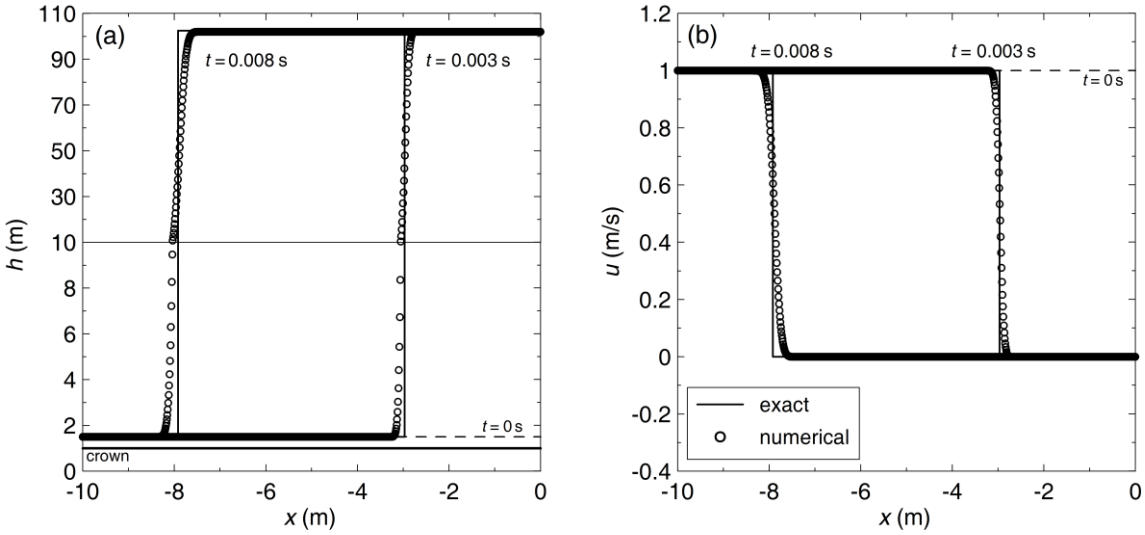

Fig. 7. Test 1c: comparison between exact solution (pressure wave speed of approximately 990 m/s) and numerical results ($\Delta x = 0.01$ m, $k_x = 10^{-7}$, $\Delta y = 0.10$ m, $k_y = 10^{-5}$, $Cr = 0.9$) at $t = 0.003$ s and $t = 0.008$ s; (a) pressure head, (b) velocity. Only the sub-domain [−10, 0] m is represented for clarity.

4.2 2D test cases with reference solution

The capability of the proposed model to predict 2D transient mixed flows is assessed in this subsection. In literature, numerical schemes based on the 2D shallow water equations are often validated by comparison with dam-break test cases with cylindrical symmetry, namely the circular dam-break and shock-focusing problems (e.g. [1,18,28]). In this work, these well-known test cases are modified in order to set up 2D discontinuous initial-value problems capable to induce propagation phenomena involving transitions between free surface and pressurized flow. Table 6 summarizes the test conditions for the two cases here considered.

Table 6 Test conditions for two 2D discontinuous initial-value problems with reference solution.

Test	Domain extension (m)	h_L (m)	u_L (m/s)	h_R (m)	u_R (m/s)	R (m)	H (m)	Description
2a	[25, 50] × [25, 50]	10.0	0.0	1.0	0.0	11.0	5.0	Mixed circular dam-break problem

2b	[0, 1.5] × [0, 1.5]	0.2	0.0	1.0	0.0	0.35	1.03	Mixed shock-focusing problem

In the original circular dam-break test case (see [18]), a 10 m-high water column with radius equal to 11 m is placed in the middle of a square 50 m × 50 m, horizontal and frictionless domain. Around, there is quiescent water with initial depth of 1 m. In this work, a 5 m-high ceiling is introduced over the whole domain (Test 2a), in such a way that the central part of the domain is initially pressurized. The sudden release of the water column generates a wave system characterized by a flow regime transition. Given the cylindrical symmetry of the problem, a 1D radial solution can be obtained by solving the following 1D system:

$$\frac{\partial \mathbf{U}}{\partial t} + \frac{\partial \mathbf{F}}{\partial r} = \mathbf{S}_r \,, \tag{33}$$

where

$$\mathbf{U} = \begin{bmatrix} \tilde{h} \\ u_r \tilde{h} \end{bmatrix}, \quad \mathbf{F} = \begin{bmatrix} u_r \tilde{h} \\ u_r^2 \tilde{h} + \dfrac{g}{2k_r}\left\{\tilde{h}^2 + H^2(k_r - 1)\right\} \end{bmatrix}, \quad \mathbf{S}_r = -\frac{1}{r}\begin{bmatrix} u_r \tilde{h} \\ u_r^2 \tilde{h} \end{bmatrix}, \tag{34}$$

$\mathbf{S}_r$ being the source term induced by the metrics. In Eq. (34), r is the radial coordinate, u_r is the radial velocity, and $\tilde{h}$ is an average depth defined as $H + k_r (h - H)$, being k_r the ratio between the length of the free surface arch and the circumferential length at a fixed radial distance. Accordingly, k_r is a geometrical parameter denoting the dimensionless slot width if $\tilde{h} > H$; it reduces to unity if $\tilde{h} \le H$. Actually, a 1D radial solution obtained from a very fine mesh can be considered a good approximation of the exact solution. Fig. 8 shows the comparison between 1D radial solution and diagonal ($y = x$) pressure head and velocity profiles computed by the fully 2D model at some selected times (t = 0.1, 0.3, and 0.7 s). The reference radial solution is obtained by numerically solving Eqs. (33)-(34) over the domain [25, 50] m discretized through a very fine uniform mesh consisting of 4000 cells. Due to axial symmetry, the 2D simulation is restricted to the sub-domain [25, 50] m × [25, 50] m, that is divided into 501 × 501 uniform computational cells. The Courant number is set equal to 0.9 in Eq. (31). From the cylindrical symmetry of the problem, it ensues that no preferential streamwise direction is recognizable *a priori* in the 2D simulation. Therefore, it is reasonable to adopt the same slot size for both systems of parallel slots aligned along the Cartesian axes ($k_x = k_y = 0.01$). Moreover, in order to make the 1D radial solution obtained by adding a single longitudinal slot comparable with the fully 2D solution computed in the presence of a lattice of orthogonal slots, the width of the single 1D slot is assumed to be double the size of each group of parallel slots in the fully 2D modeling. In this way, the two models ideally make available the same supplementary volume above the conduit crown. Fig. 8 highlights that the 2D numerical results fit fairly well the reference solution and that the 2D model is capable of satisfactorily reproducing both the depressurization of the water

column generated by the inward-propagating rarefaction wave and the evolution of the following fully free surface flow with a circular shock wave expanding outwards. Since axial and diagonal profiles are nearly undistinguishable, only diagonal profiles are shown in Fig. 8 for the sake of clarity. Hence, the 2D numerical solution excellently preserves the circular symmetry despite the Cartesian mesh.

The classic shock-focusing test case is commonly defined in a dimensionless context (see, for example, [18]). In this work, an analogous test (Test 2b) is carried out on a dimensional square domain $[-1.5, 1.5]$ m × $[-1.5, 1.5]$ m, again horizontal and frictionless. An idealized circular dam of radius 0.35 m is placed in the center of the domain, and a static condition is initially assumed with the water depth equal to 0.2 m inside the dam and 1 m outside. The sudden removal of the idealized dam induces a circular shock wave moving towards the center and an outward-propagating rarefaction wave. The shock progressively concentrates and "implodes" in the focusing point (0, 0). It is proved in literature that this collision process causes strong numerical difficulties to 2D models, especially if a Cartesian mesh is adopted (e.g. [19]). In the revised version of the shock-focusing test case here considered, the implosion in the focusing point is exploited to generate a 2D transient mixed flow. With this aim, a 1.03 m-high ceiling is introduced throughout the domain. Accordingly, the shock collision produces a strong pressurization near the focusing point and gives origin to a circular filling bore which expands outwards. The 2D simulation is restricted to the [0, 1.5] m × [0, 1.5] m sub-domain and is performed by setting the model parameters as follows: $\Delta x = \Delta y = 3$ mm, $k_x = k_y = 0.01$, $Cr = 0.9$. Again, thanks to the cylindrical symmetry of the problem, a reference solution is obtained by solving Eqs. (33)-(34) on the sub-domain [0, 1.5] m with a fine mesh of 3000 cells; the dimensionless slot width is assumed equal to 0.02 for the reason explained above. Fig. 9 shows the comparison between 1D radial solution and diagonal ($y = x$) pressure head and velocity profiles at some selected times ($t = 0.05, 0.10, 0.15$ s). The good agreement between reference 1D and 2D results confirms the effectiveness and robustness of the fully 2D model, even for this extremely severe test case. In particular, a fairly good description of the propagating phenomenon immediately after the collision is provided by the 2D model, even though some discrepancies arise in the peak values (see the profiles at $t = 0.10$ s). Axial profiles are omitted in Fig. 9 because, also in this case, circular symmetry is preserved very well.

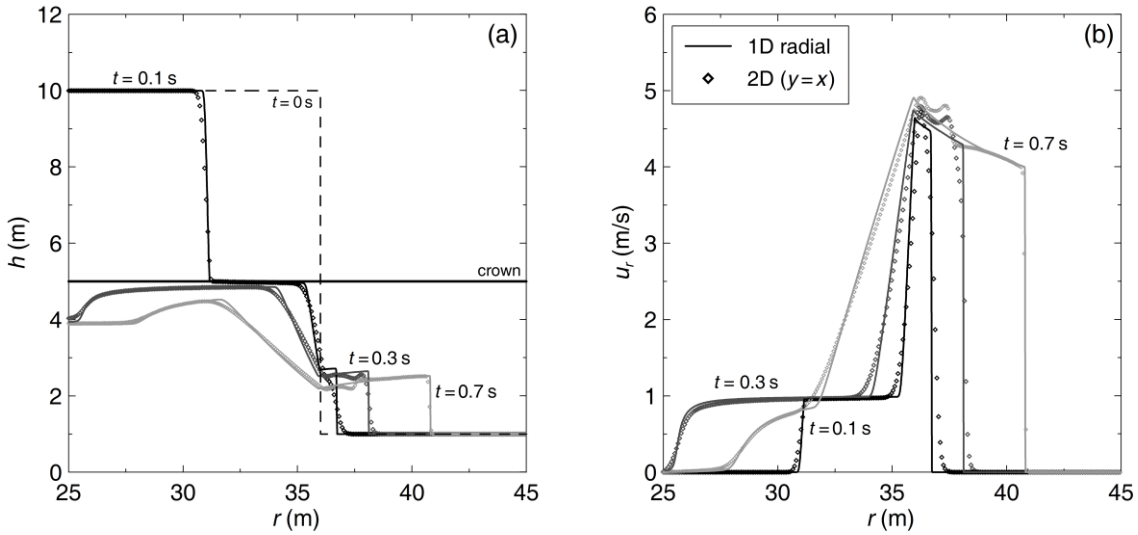

Fig. 8. Test 2a: comparison between reference 1D radial solution (4000 cells) and 2D numerical profiles along $y = x$ (501 × 501 cells) at $t = 0.1$ s, $t = 0.3$ s, and $t = 0.7$ s; (a) pressure head, (b) velocity. Only the radial sub-domain [25, 45] m is represented for clarity.

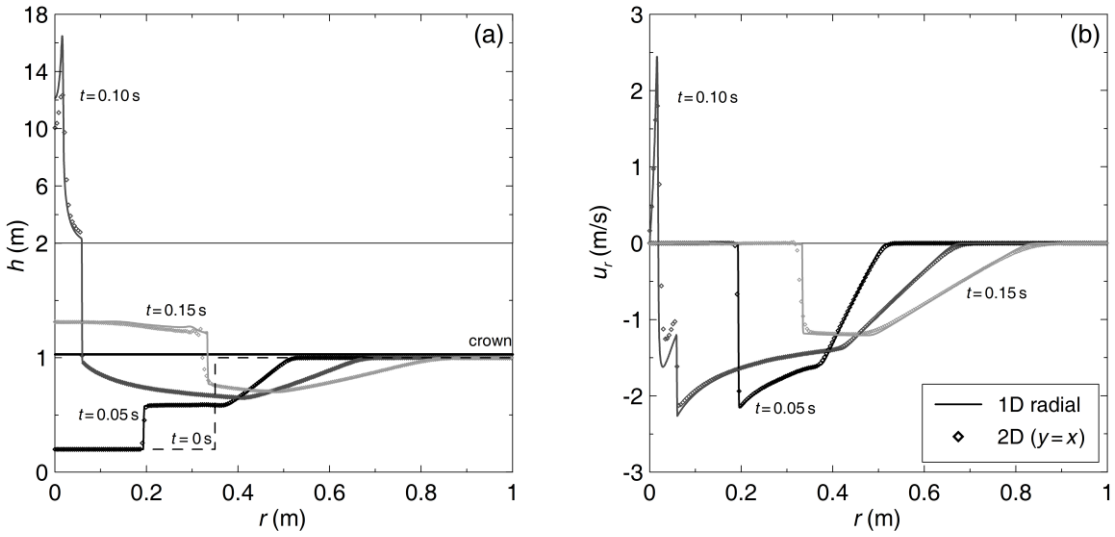

Fig. 9. Test 2b: comparison between reference 1D radial solution (3000 cells) and 2D numerical profiles along $y = x$ (501 × 501 cells) at $t = 0.05$ s, $t = 0.10$ s, and $t = 0.15$ s; (a) pressure head, (b) velocity. Only the radial sub-domain [0, 1] m is represented for clarity.

4.3. A field-scale test case

In order to assess the suitability of the model to be applied to real case studies, the transit of a dam-break bore under an arch bridge is here modeled. This specific situation is quite interesting because, in practical applications, the presence of hydraulic structures, such as bridges or culverts, that could be partially or fully pressurized during a flood, could strongly affect the near-field flow. Accordingly, attention has been recently devoted in literature to the

development of methodologies that take into account this kind of structures in 2D numerical modeling (see, for example, [22]).

The test case here considered concerns a straight horizontal channel of length 500 m with a 20 m-wide rectangular cross-section (Fig. 10). An ideal thin vertical wall (simulating a retaining structure) identifies an upstream channel reach with length of 200 m. A 20 m-wide arch bridge, located 50 m downstream of the wall, crosses over the canal perpendicularly to its center line. It is characterized by a parabolic lower profile described by the equation: $H = -0.04\,y^2 + 0.8\,y + 4$, where H indicates the elevation of the ceiling and y the transverse coordinate. The upstream channel reach initially acts as a reservoir containing still water with a depth of 15 m. Downstream, the bed is initially wet with a layer of still water 1.5 m deep. The sudden collapse of the wall induces the formation of a bore moving downstream towards the bridge. This test case represents a schematization of a real situation; nevertheless, despite the schematic geometry, it is useful to verify the model reliability in this kind of engineering applications.

The computational domain is discretized by means of a Cartesian mesh with cell size $\Delta x = 1$ m $\times$ $\Delta y = 0.5$ m. An orthogonal lattice of slots with dimensionless widths k_x and k_y both equal to 0.01 is ideally introduced over the lower surface of the bridge. Bed resistance is included in this case by setting the Manning roughness coefficient at 0.03 s m$^{-1/3}$, whereas the resistance effects due to the lateral walls and the lower surface of the bridge are neglected. Finally, the Courant number is assumed equal to 0.9.

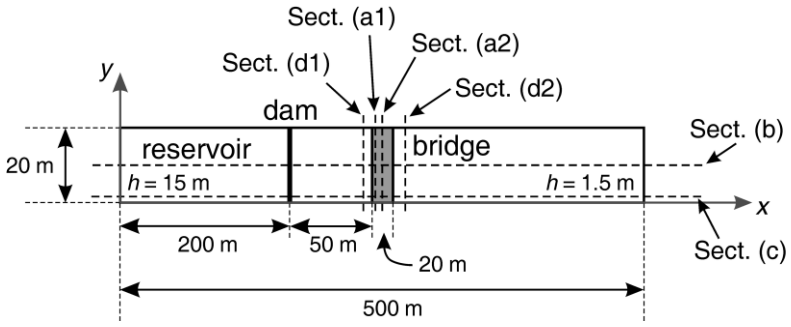

Sect. (a1)	$x = 251.5$ m
Sect. (a2)	$x = 259.5$ m
Sect. (b)	$y = 9.75$ m
Sect. (c)	$y = 1.75$ m
Sect. (d1)	$x = 245.5$ m
Sect. (d2)	$x = 279.5$ m

Fig. 10. Plan view sketch of the idealized field-scale test case. Cross-sections are selected along computational cell centers.

As an example of model results, Fig. 11 shows some computed cross-sectional (Fig. 11a and d) and longitudinal (Fig. 11b and c) profiles for pressure head at $t = 10$ s. At the time considered, the bore has already passed beyond the bridge and keeps propagating downward. The opening under the bridge is partially pressurized (Fig. 10e). Predicted transverse pressure head profiles along the bridge show a peculiar "U" shape, even associated with highly different values between the center line and the sides of the channel. Moreover, the presence of the arc structure gives origin to

2D near-field effects: a wake and a backwater effect develop behind and in front of the bridge, respectively. This justifies the adoption of a 2D mixed flow model to describe the flow field near the bridge.

Despite the fact that a reference solution is not available for comparison, the numerical results confirm the applicability of the 2D Preissmann slot model to field-scale problems characterized by the presence of topographic singularities (such as culverts or bridges) that could locally induce the pressurization of the flow.

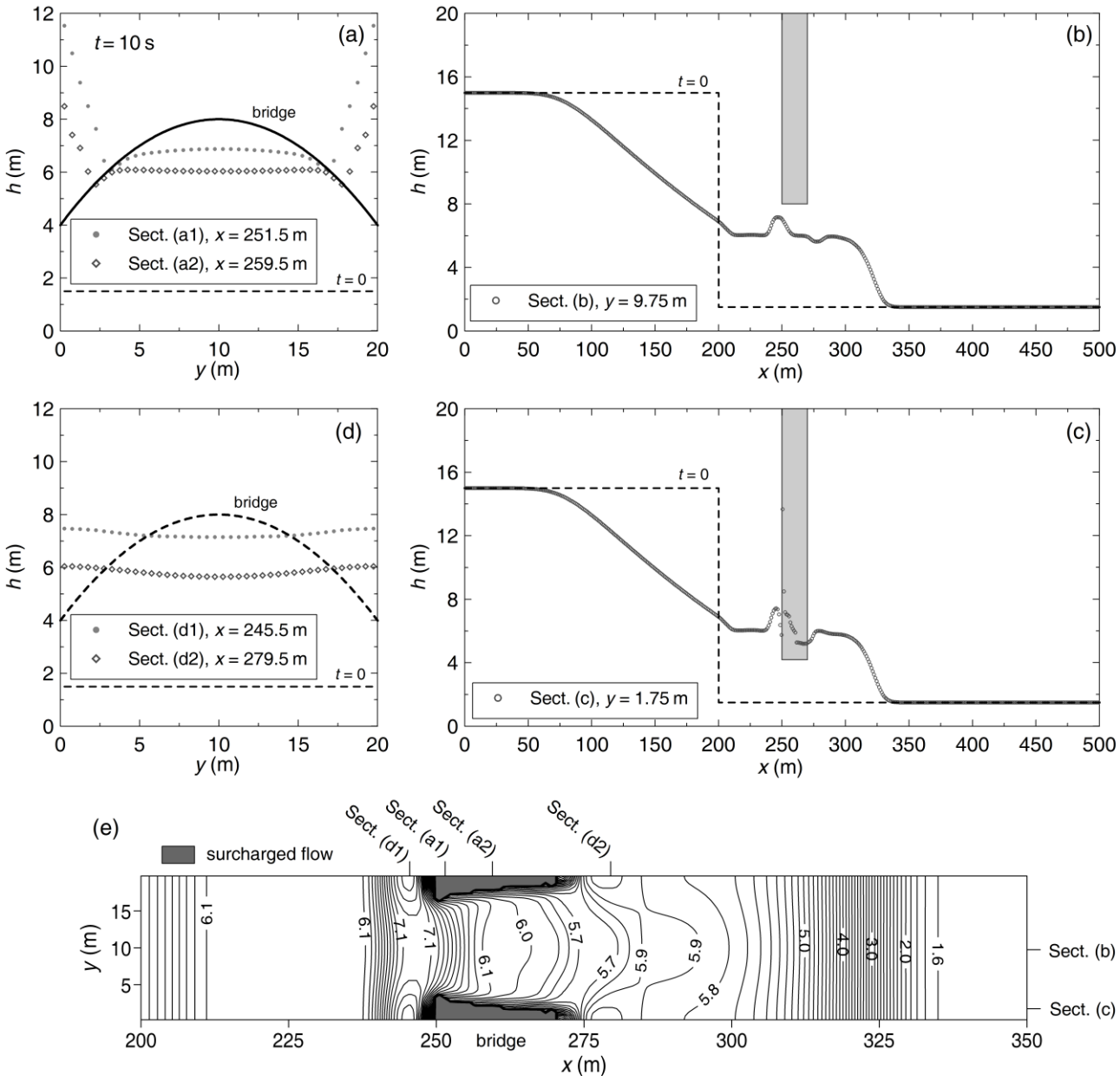

Fig. 11. Transit of a dam-break bore under an arch bridge: numerical results at $t = 10$ s obtained by setting $k_x = k_y = 0.01$. a) Pressure head cross-sectional profiles in correspondence of the bridge (at $x = 251.5$ m and $x = 259.5$ m). b) Pressure head longitudinal profile at the channel center line ($y = 9.75$ m). c) Pressure head longitudinal profile at the channel side ($y = 0.25$ m). d) Water depth cross-sectional profiles just upstream ($x = 245.5$ m) and

downstream (x = 279.5 m) of the bridge. e) Water depth contour map for a channel stretch including the bridge (contour levels in m) and prediction of surcharged and free surface areas in the culverted reach.

5. Conclusions

In this paper the Preissmann slot concept is extended and applied to 2D highly transient mixed flows. The resulting shallow water model, coupled with a Godunov-type finite volume numerical scheme, is capable to correctly reproduce both exact solutions of 1D discontinuous initial value problems and reference radial solutions of idealized cylindrically symmetric test cases, characterized by either abrupt or mild transitions between free surface and surcharged flows.

The field-scale simulation of the transit of a bore under an arch-bridge confirms the reliability and robustness of the model in practical applications involving topographical singularities, as bridges or culverts, that could be partially or totally filled during flood events.

In numerical simulation of 2D problems, since a preferential direction for the flow cannot be identified *a priori*, it seems reasonable to adopt the same value of the slot width to grid size ratio for both systems of orthogonal slots. Numerical results show that a good compromise between accuracy and computational stability, especially when strong pressurization waves occur, is guaranteed by setting this dimensionless ratio in the order of 1%.

An interesting perspective of this work lies in the possibility of limiting the slot height and restoring the current cell dimensions above the slot lattice. This adjustment could allow modeling the overflowing of a bridge and similar overtopping processes by a simple adaptation of geometrical expressions. However, the suitability of the Preissmann model could be poor in some cases, due to the fact that the shallow water approximation is not fully satisfied in the near-field flow. In flooding phenomena, for example, the flow over a long culvert may even be totally separate from the culvert flow itself. Due to its practical relevance, this extension is nowadays in progress.

Acknowledgements

The reviewers are kindly acknowledged for their valuable comments which have greatly contributed to the improvement of the paper.

References

[1] Alcrudo F, Garcia-Navarro P. A high-resolution Godunov-type scheme in finite volumes for the 2D shallow-water equations. Int J Numer Meth Fluids 1993; 16(6):489–505. http://dx.doi.org/10.1002/fld.1650160604.

[2] Aureli F, Maranzoni A, Mignosa P, Ziveri C. A weighted surface-depth gradient method for the numerical integration of the 2D shallow water equations with topography. Adv Water Res 2008;31(7):962–74. http://dx.doi.org/10.1016/j.advwatres.2008.03.005.

[3] Bourdarias C, Gerbi S. A finite volume scheme for a model coupling free surface and pressurized flows in pipes. J Comput Appl Math 2007;209(1):109–31. http://dx.doi.org/10.1016/j.cam.2006.10.086.

[4] Bousso S, Daynou M, Fuamba M. Numerical modeling of mixed flows in storm water systems: critical review of literature. J Hydraul Eng 2013;139(4):385–96. http://dx.doi.org/10.1061/(ASCE)HY.1943-7900.0000680.

[5] Bousso S, Fuamba M. Numerical and experimental analysis of the pressurized wave front in a circular pipe. J Hydraul Eng 2014;140(3):300–12. http://dx.doi.org/10.1061/(ASCE)HY.1943-7900.0000827.

[6] Capart H, Sillen X, Zech Y. Numerical and experimental water transients in sewer pipes. J Hydraul Res 1997;35(5):659–72. http://dx.doi.org/10.1080/00221689709498400.

[7] Cardle JA, Song CCS, Yuan M. Measurements of mixed transient flows. J Hydraul Eng 1989;115(2):169–82. http://dx.doi.org/10.1061/(ASCE)0733-9429(1989)115:2(169).

[8] Cataño-Lopera Y, Tokyay T, Martin J, Schmidt A, Lanyon R, Fitzpatrick K, Scalise C, García M. Modeling of a transient event in the tunnel and reservoir plan system in Chicago, Illinois. J Hydraul Eng 2014;140(9):05014005. http://dx.doi.org/10.1061/(ASCE)HY.1943-7900.0000888.

[9] Cunge JA, Wegner M. Numerical integration of Barré de Saint-Venant's flow equations by means of an implicit scheme of finite differences." La Houille Blanche 1964;1:33–39. http://dx.doi.org/10.1051/lhb/1964002.

[10] García-Navarro P, Alcrudo F, Priestley A. An implicit method for water flow modelling in channels and pipes. J Hydraul Res 1994;32(5):721–42. http://dx.doi.org/10.1080/00221689409498711.

[11] Kerger F, Archambeau P, Erpicum S, Dewals BJ, Pirotton M. An exact Riemann solver and a Godunov scheme for simulating highly transient mixed flows. J Comput Appl Math 2011;235(8):2030–40. http://dx.doi.org/10.1016/j.cam.2010.09.026.

[12] Kerger F, Archambeau P, Dewals BJ, Erpicum S, Pirotton M. Three-phase bi-layer model for simulating mixed flows. J Hydraul Res 2012;50(3):312–19. http://dx.doi.org/10.1080/00221686.2012.684454.

[13] León AS, Ghidaoui MS, Schmidt AR, García MH. Godunov-type solutions for transient flows in sewers. J Hydraul Eng 2006;132(8):800–13. http://dx.doi.org/10.1061/(ASCE)0733-9429(2006)132:8(800).

[14] León AS, Ghidaoui MS, Schmidt AR, García MH. Application of Godunov-type schemes to transient mixed flows. J Hydraul Res 2009;47(2):147–56. http://dx.doi.org/10.3826/jhr.2009.3157.

[15] León AS, Ghidaoui MS, Schmidt AR, García MH. A robust two-equation model for transient-mixed flows. J Hydraul Res 2010;48(1):44–56. http://dx.doi.org/ 10.1080/00221680903565911.

[16] LeVeque RJ. Finite volume methods for hyperbolic problems. Cambridge, UK: Cambridge University Press; 2002.

[17] Li J, McCorquodale A. Modeling mixed flow in storm sewers. J Hydraul Eng 1999;125(11):1170–80. http://dx.doi.org/10.1061/(ASCE)0733-9429(1999)125:11(1170).

[18] Liska R, Wendroff B. Two-dimensional shallow water equations by composite schemes. Int J Numer Meth Fluids 1999;30(4):461–79. http://dx.doi.org/10.1002/(SICI)1097-0363(19990630)30:4<461::AID-FLD850>3.0.CO;2-4.

[19] Morel AT, Fey M, Maurer J. Multidimensional high order method of transport for the shallow water equations. Research Report No. 96-09 1996; ETH Zurich, Switzerland.

[20] Noto L, Tucciarelli T. DORA algorithm for network flow models with improved stability and convergence properties. J Hydraul Eng 2001;127(5):380–91. http://dx.doi.org/10.1061/(ASCE)0733-9429(2001)127:5(380).

[21] Politano M, Odgaard AJ, Klecan W. Case study: numerical evaluation of hydraulic transients in a combined sewer overflow tunnel system. J Hydraul Eng 2007;133(10):1103–10. http://dx.doi.org/10.1061/(ASCE)0733-9429(2007)133:10(1103).

[22] Ratia H, Murillo J, García-Navarro P. Numerical modelling of bridges in 2D shallow water flow simulations. Int J Numer Meth Fluids 2014;75(4):250–72. http://dx.doi.org/10.1002/fld.3892.

[23] Sabbagh-Yazdi SR, Mastorakis NE, Abbasi A. Water hammer modeling by Godunov type finite volume method. Int J Math Comput Sim 2007;1(4):350–55. http://www.naun.org/main/NAUN//mcs/mcs-56.pdf.

[24] Sanders BF, Bradford SF. Network implementation of the two-component pressure approach for transient flow in storm sewers. J Hydraul Eng 2011;137(2):158–72. http://dx.doi.org/10.1061/(ASCE)HY.1943-7900.0000293.

[25] Song CCS, Cardle JA, Leung KS. Transient mixed-flow models for storm sewers. J Hydraul Eng 1983;109(11):1487–504. http://dx.doi.org/10.1061/(ASCE)0733-9429(1983)109:11(1487).

[26] Syme WJ, Pinnell MG, Wicks JM. Modelling flood inundation of urban areas in the UK using 2D/1D hydraulic models. In: 8th Australian Conference on Hydraulics in Water Engineering, IEAust., Gold Coast, Australia; 2004.

[27] Toro EF. Riemann solvers and numerical methods for fluid dynamics. 2nd edition. Berlin, Germany: Springer; 1999.

[28] Toro EF. Shock-capturing methods for free-surface shallow flows. Chichester, England: John Wiley & Sons; 2001.

[29] Trajkovic B, Ivetic M, Calomino F, D'Ippolito A. Investigation of transition from surface to pressurized flow in a circular pipe. Water Sci Technol 1999;39(9):105–12. http://dx.doi.org/10.1016/S0273-1223(99)00222-X.

[30] Trindade BC, Vasconcelos JG. Modeling of water pipeline filling events accounting for air phase interactions. J Hydraul Eng 2013;139(9):921–34. http://dx.doi.org/10.1061/(ASCE)HY.1943-7900.0000757.

[31] Van Leer B. Towards the ultimate conservative difference scheme. II. Monotonicity and conservation combined in second order scheme. J Comput Phys 1974;14(4):361–70. http://dx.doi.org/10.1016/0021-9991(74)90019-9.

[32] Van Nam N, Erpicum S, Dewals BJ, Pirotton M, Archambeau P. Experimental investigations of 2D stationary mixed flows and numerical comparison. In: Proc. 2nd IAHR Europe Congress, Munich, Germany; 2012.

[33] Vasconcelos JG, Wright SJ, Roe PL. Improved simulation of flow regime transition in sewers: the two-component pressure approach. J Hydraul Eng 2006;132(6):553–62. http://dx.doi.org/10.1061/(ASCE)0733-9429(2006)132:6(553).

[34] Vasconcelos JG, Wright SJ. Comparison between the two-component pressure approach and current transient flow solvers. J Hydraul Res 2007;45(2):178–87. http://dx.doi.org/10.1080/00221686.2007.9521758.

[35] Vasconcelos JG, Wright SJ. Investigation of rapid filling of poorly ventilated stormwater storage tunnels. J Hydraul Res 2009;47(5):547–58. http://dx.doi.org/10.3826/jhr.2009.3390.

[36] Vasconcelos JG, Wright SJ, Roe PL. Numerical oscillations in pipe-filling bore predictions by shock-capturing models. J Hydraul Eng 2009;135(4):296–305. http://dx.doi.org/10.1061/(ASCE)0733-9429(2009)135:4(296).

[37] Wiggert DC. Transient flow in free-surface, pressurized systems. J Hydraul Div 1972;98(1):11–27.

[38] Zhao M, Ghidaoui MS. Godunov-type solutions for water hammer flows. J Hydraul Eng 2004;130(4):341–48. http://dx.doi.org/10.1061/(ASCE)0733-9429(2004)130:4(341).

[39] Zhou F, Hicks FE, Steffler PM. Transient flow in a rapidly filling horizontal pipe containing trapped air. J Hydraul Eng 2002;128(6):625–34. http://dx.doi.org/10.1061/(ASCE)0733-9429(2002)128:6(625).

List of figure captions

Figure 1 – Definition sketch of the 2D elemental Cartesian control volume with the addition of two narrow vertical slots on the top: flow involving (a) or not involving (b) the slots.

Figure 2 – Test 1a: exact solutions at $t = 0.5$ s and $t = 1.0$ s calculated with different values of the slot width (channel width $B = 1$ m); (a) pressure head, (b) velocity. $T_y = 0$ refers to the solution obtained by applying the Rankine-Hugoniot relations. The other theoretical profiles are computed using an exact Riemann solver. Only the sub-domain [−10, 0] m is represented for clarity.

Figure 3 – Test 1a: comparison between theoretical solution provided by the exact Riemann solver and numerical results at $t = 0.5$ s and $t = 1$ s; (a) pressure head, (b) velocity. Two data series are reported, corresponding to $k_y = 0.01$ and $k_y = 0.1$ respectively (settings of the model parameters: $\Delta x = 0.01$ m, $k_x = 0.001$, $\Delta y = 0.10$ m, $Cr = 0.9$). Only the sub-domain [−10, 0] m is represented for clarity.

Figure 4 – Test 1a: convergence analysis based on three different longitudinal grid sizes (Δx = 0.01, 0.05, and 0.10 m). Pressure head (a) and velocity (b) profiles at t = 0.5 s are shown (k_x = 0.001, Δy = 0.10 m, k_y = 0.01, Cr = 0.9). The x-axis is limited to the interval [−4, −3.2] for clarity.

Figure 5 – Test 1a: sensitivity analysis with respect to the width of the transverse slot ($k_x = 10^{-2}$, 10^{-3}, and 10^{-4}). Pressure head (a) and velocity (b) profiles at t = 0.5 s are shown (Δx = 0.01 m, Δy = 0.10 m, k_y = 0.01, Cr = 0.9). The x-axis is limited to the interval [−4, −3.2] for clarity.

Figure 6 – Test 1b: comparison between exact solution and numerical results at t = 0.3 s (Δx = 0.01 m, Δy = 0.10 m, k_y = 0.01, Cr = 0.9); (a) pressure head, (b) velocity. Profiles obtained by setting two different widths for the transverse slot ($k_x = 10^{-3}$ and 10^{-4}) are shown. Only the sub-domain [−10, 2] m is represented for clarity.

Figure 7 – Test 1c: comparison between exact solution (pressure wave speed of approximately 990 m/s) and numerical results (Δx = 0.01 m, $k_x = 10^{-7}$, Δy = 0.10 m, $k_y = 10^{-5}$, Cr = 0.9) at t = 0.003 s and t = 0.008 s; (a) pressure head, (b) velocity. Only the sub-domain [−10, 0] m is represented for clarity.

Figure 8 – Test 2a: comparison between reference 1D radial solution (4000 cells) and 2D numerical profiles along $y = x$ (501 × 501 cells) at t = 0.1 s, t = 0.3 s, and t = 0.7 s; (a) pressure head, (b) velocity. Only the radial sub-domain [25, 45] m is represented for clarity.

Figure 9 – Test 2b: comparison between reference 1D radial solution (3000 cells) and 2D numerical profiles along $y = x$ (501 × 501 cells) at t = 0.05 s, t = 0.10 s, and t = 0.15 s; (a) pressure head, (b) velocity. Only the radial sub-domain [0, 1] m is represented for clarity.

Figure 10 – Plan view sketch of the idealized field-scale test case. Cross-sections are selected along computational cell centers.

Figure 11 – Transit of a dam-break bore under an arch bridge: numerical results at t = 10 s obtained by setting $k_x = k_y$ = 0.01. a) Pressure head cross-sectional profiles in correspondence of the bridge (at x = 251.5 m and x = 259.5 m). b) Pressure head longitudinal profile at the channel center line (y = 9.75 m). c) Pressure head longitudinal profile at the channel side (y = 0.25 m). d) Water depth cross-sectional profiles just upstream (x = 245.5 m) and downstream (x = 279.5 m) of the bridge. e) Water depth contour map for a channel stretch including the bridge (contour levels in m) and prediction of surcharged and free surface areas in the culverted reach.

List of table captions

Table 1 – Test conditions for three 1D discontinuous initial-value problems with exact solution (computational domain defined by [−10, 10] m × [0, 1] m and initial discontinuity located at x = 0 m).

Table 2 – Test 1a: sensitivity of the solution provided by the exact Riemann solver by Kerger et al. [11] to the width of the Preissmann slot. Relative percent deviations are referred to the analytical solution derived from the application of the Rankine-Hugoniot conditions. The volume fraction contained within the slot with respect to the overall water volume in the duct is reported for t = 0.5 s and t = 1.0 s.

Table 3 – Test 1a: sensitivity analysis on longitudinal grid size based on the pressure head and velocity profiles at t = 0.5 s. The L_1-norms are calculated with respect to the exact solution over the half computational domain [−10, 0] m.

Table 4 – Test 1a: sensitivity analysis on the k_x parameter based on the pressure head and velocity profiles at t = 0.5 s (k_y = 0.01). The L_1-norms are calculated with respect to the exact solution over the half computational domain [−10, 0] m.

Table 5 – Test 1b: sensitivity analysis on longitudinal grid size based on the pressure head and velocity profiles at t = 0.3 s ($k_y = 10^{-2}$, $k_x = 10^{-4}$). The L_1-norms are calculated with respect to the exact solution over the total computational domain [−10, 10] m.

Table 6 – Test conditions for two 2D discontinuous initial-value problems with reference solution.